Monthly Notices
of the
ROYAL ASTRONOMICAL SOCIETY

MNRAS **485,** 924–933 (2019) doi:10.1093/mnras/stz407

Magnetic field and ISM in the local Galactic disc

Y. Sofue,[1]★ H. Nakanishi[2] and K. Ichiki[3]

[1]*Institute of Astronomy, The University of Tokyo, Tokyo 181-0015, Japan*
[2]*Graduate Schools of Science and Engineering, Kagoshima University, Kagoshima 890-8544, Japan*
[3]*Graduate School of Science, Division of Particle and Astrophysical Science, Nagoya University, Nagoya 464-8602, Japan*

Accepted 2019 February 3. Received 2019 January 25; in original form 2018 December 28

ABSTRACT

A correlation analysis is obtained among Faraday rotation measure, H I column density, and thermal and synchrotron radio brightness using archival all-sky maps of the Galaxy. A method is presented to calculate the magnetic strength and its line-of-sight (LOS) component, volume gas densities, effective LOS depth, and effective scale height of the disc from these data in a hybrid way. Applying the method to archival data, all-sky maps of the local magnetic field strength and its parallel component are obtained, which reveal details of local field orientation.

Key words: galaxies: individual (Milky Way) – ISM: general – ISM: magnetic field.

1 INTRODUCTION

Large-scale mappings of the Faraday rotation measure (RM) of extragalactic linearly polarized radio sources have been achieved extensively in recent decades (Taylor, Stil & Sunstrum 2009; Oppermann et al. 2012), with which various analyses have been obtained to investigate structures of galactic as well as intergalactic magnetic fields (see e.g. the review by Akahori et al. 2018).

Local magnetic fields in the Solar vicinity have also been studied using these RM data as well as polarization observations of the Galactic radio emission (Wolleben et al. 2010; Stil, Taylor & Sunstrum 2011; Mao et al. 2012; Sun et al. 2015; Sofue & Nakanishi 2017; Liu et al. 2017; Van Eck et al. 2017; Alves et al. 2018).

Synchrotron radio emission is a tool to measure the total strength of a magnetic field on the assumption that the magnetic energy density (pressure) is in equipartition with the thermal and cosmic ray energy densities (e.g. Sofue, Fujimoto & Wielebinski 1986). This method requires information about the depth of the emitting region in order to calculate the synchrotron emissivity per volume, as the intensity is an integration of the emissivity along the line of sight (LOS).

The rotation measure is an integration of the parallel component of the magnetic field multiplied by thermal electron density along the line of sight (LOS). It is related not only to thermal (free–free) radio emission, but also to H I column density through the thermal electron fraction in the neutral interstellar medium (ISM).

Determination of the LOS depth is therefore key to the measurement of the magnetic strength from synchrotron emission and the parallel magnetic component from the RM. The depth is also required to estimate the volume densities of H I and thermal electrons from observed H I and thermal radio intensities. The emission measure and H I column density are useful to estimate the LOS depth, given that a relation between the thermal and H I gas densities is appropriately settled.

In this paper, correlation analyses are obtained among various radio astronomical observables (RM, H I column density, thermal and synchrotron radio brightness) in order to determine physical quantities of the ISM such as the magnetic strength, gas densities, and LOS depth. One of the major goals of the present hybrid analysis method is to obtain whole-sky maps of the total strength and parallel component of the magnetic field in the local Galactic disc.

2 OBSERVABLES AND CORRELATIONS

2.1 Data

The observational data for the Faraday rotation were taken from the all-sky RM survey by Taylor et al. (2009), H I data from the Leiden–Argentine–Bonn (LAB) survey by Kalberla et al. (2005), and synchrotron and free–free emissions at 23 GHz from the seven-year result of the W*ilkinson Microwave Anisotropy Probe* (*WMAP*) project by Gold et al. (2011). Fig. 1 shows the employed map data for *RM*, |*RM*|, H I column density $N_{\rm HI}$, thermal (free–free) radio brightness temperature $T_{\rm ff}$ and synchrotron radio brightness $T_{\rm syn}$, the latter two both at 23 GHz.

Fig. 2 shows plots of the same data in Fig. 1 against the latitude b and cosec $|b|$. The global similarity of the latitudinal variations indicates that the four observed quantities are deeply coupled with each other. It is remarkable that all the plots beautifully obey the cosec $|b|$ relation shown by the full lines. This fact indicates that these radio-observed quantities are tightly coupled with the line-of-sight depth (LOS) through a galactic disc composed of a plane-parallel layer in the first approximation.

A more detailed inspection of the figures reveals that, besides the global common cosec $|b|$ property, there exist systematic differences in the latitudinal variations among the quantities. The rotation measure, *RM*, shows a weaker increase toward the galactic plane

★ E-mail: sofue@ioa.s.u-tokyo.ac.jp

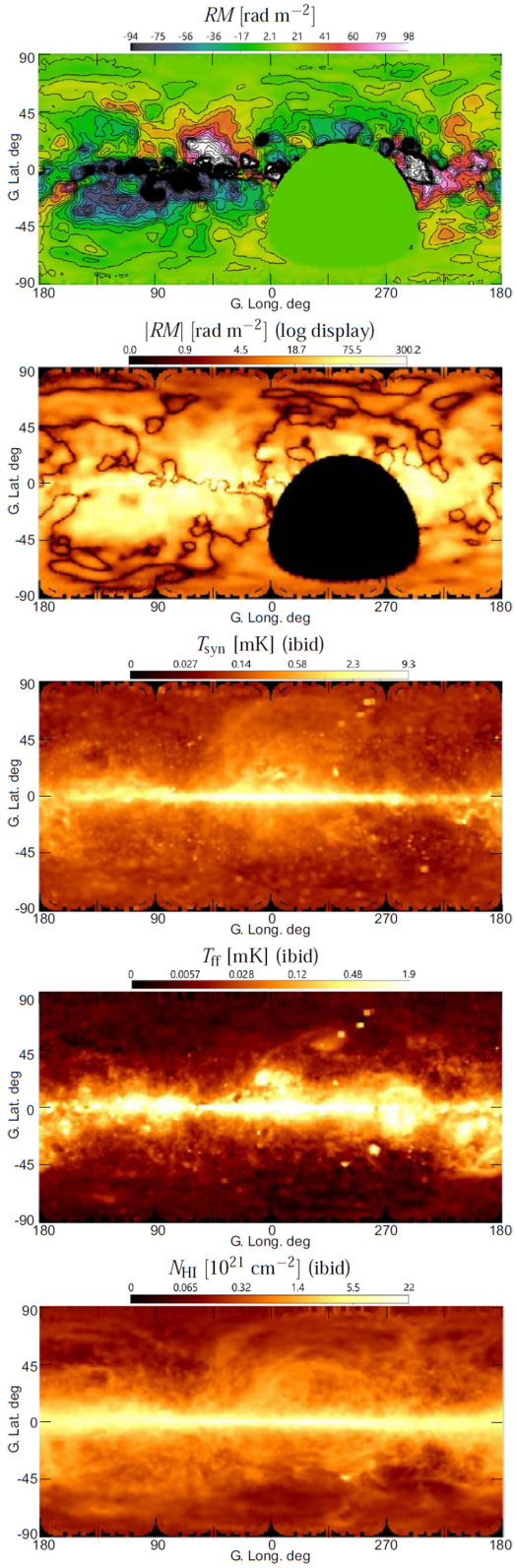

Figure 1. All-sky maps of *RM*, $|RM|$ (rad m^{-2}) (Taylor et al. 2009), $T_{\rm syn}$ and $T_{\rm ff}$ (mK) at 23 GHz (Gold et al. 2011), and $N_{\rm HI}$ (10^{21} cm^{-2}) (Kalberla et al. 2005).

than the other quantities. The saturation of $|RM|$ near the galactic plane suggests that the magnetic field directions are reversing there. On the other hand, the synchrotron intensity has a much sharper peak at the plane, and shows a similar variation to the H I intensity. Another remarkable property is the sharper increase of the thermal emission toward the galactic plane than H I. This manifests the stronger dependence of the thermal emission on the ISM density through the emission measure $EM \propto n_{\rm e}^2 L$ than that of the H I column $N_{\rm HI} \propto n_{\rm HI} L$.

The radio observables are related to the ISM quantities as follows. The Faraday rotation measure *RM* is related to the thermal electron density $n_{\rm e}$ and line-of-sight (LOS) component of the magnetic field strength $B_{//}$ through

$$\left(\frac{RM}{\rm rad\ m^{-2}}\right) \sim 0.81 \left(\frac{\langle n_{\rm e}\rangle}{\rm cm^{-3}}\right) \left(\frac{\langle B_{//}\rangle}{\mu\rm G}\right) \left(\frac{L}{\rm pc}\right). \quad (1)$$

The emission measure *EM* is rewritten by the volume density $n_{\rm e}$ of thermal electrons as

$$\left(\frac{EM}{\rm pc\ cm^{-6}}\right) \sim \left(\frac{\langle n_{\rm e}\rangle}{\rm cm^{-3}}\right)^2 \left(\frac{L}{\rm pc}\right). \quad (2)$$

The H I column density $N_{\rm HI}$ is given by the H I volume density $n_{\rm HI}$ as

$$\left(\frac{N_{\rm HI}}{\rm cm^{-2}}\right) \sim 3.086 \times 10^{18} \left(\frac{\langle n_{\rm HI}\rangle}{\rm cm^{-3}}\right) \left(\frac{L}{\rm pc}\right). \quad (3)$$

Here, $\langle\ \rangle$ denotes the LOS average, which is defined and described later. The synchrotron radio brightness Σ_ν, as observed by the brightness temperature $T_{\rm syn}$, is related to the volume emissivity ϵ, frequency ν, and L as

$$\Sigma_\nu = \frac{2kT_{\rm syn}}{\lambda^2} \sim \frac{L}{4\pi}\frac{{\rm d}\epsilon}{{\rm d}\nu} \sim \frac{L}{4\pi}\frac{\epsilon}{\nu}, \quad (4)$$

which may be rewritten in a practical way as

$$\left(\frac{T_{\rm syn}}{\rm K}\right) \sim 1.472 \times 10^{11} \left(\frac{\nu}{\rm GHz}\right)^{-3} \left(\frac{\epsilon}{\rm erg\ cm^{-3}\ s^{-1}}\right) \left(\frac{L}{\rm pc}\right), \quad (5)$$

where $\lambda = c/\nu$ is the wavelength and k is the Boltzmann constant.

We assume that the Galactic disc is composed of four horizontal layers (discs) of H I gas, thermal electrons, magnetic fields and cosmic rays, which have the same half-thickness (scale height) $z_{1/2:{\rm disc}}$. This means that the LOS depths L of the four quantities are equal. This assumption may not be good enough for the synchrotron emission that may originate from a thicker magnetic halo. However, it may be considered that the contribution of a magnetic halo to *RM* and synchrotron emission is much smaller than that of the disc because of the magnetic strength and electron density being weaker by an order of magnitude. The depth L used here is an effective depth, and is related to the geometrical depth through a volume-filling factor, as will be described later in detail.

Based on these considerations, we assume that the ISM quantities are smooth functions of the effective LOS depth L for the first approximation, and that an average of any quantity f over L satisfies the following relation:

$$\langle f\rangle = \frac{\int_0^L f\,{\rm d}x}{\int_0^L {\rm d}x} = \frac{\int_0^L f\,{\rm d}x}{L}. \quad (6)$$

We also assume for any quantities f and g

$$\langle f\rangle \sim \langle f^2\rangle^{1/2}, \quad (7)$$

and

$$\langle fg\rangle \sim \langle f\rangle\langle g\rangle. \quad (8)$$

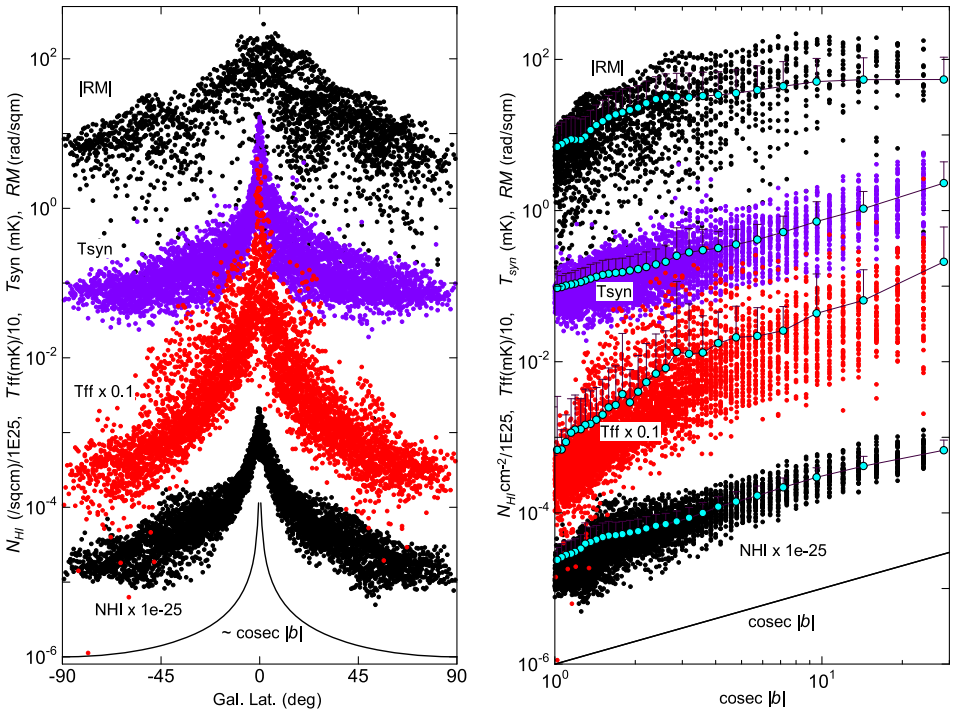

Figure 2. $|RM|$ (rad m^{-2}), $T_{\rm syn}$ (mK), 0.1 × $T_{\rm ff}$ (mK) and 10^{-25} × $N_{\rm HI}$ (cm^{-2}) plotted against latitude b. Points are reduced by 1 per 10. Note the beautiful dependence of the plotted quantities on the cosec $|b|$ relation shown by the full lines, indicating that they are tightly coupled with the line-of-sight depth of a plane-parallel layer. The right-hand panel shows the same, but against cosec $|b|$. Open circles are averages of the plots in every 2° bin of absolute latitude. Bars show standard deviations (sd) of the original values, which are given only in the upper sides in order to avoid a logarithm of negative values for large sd.

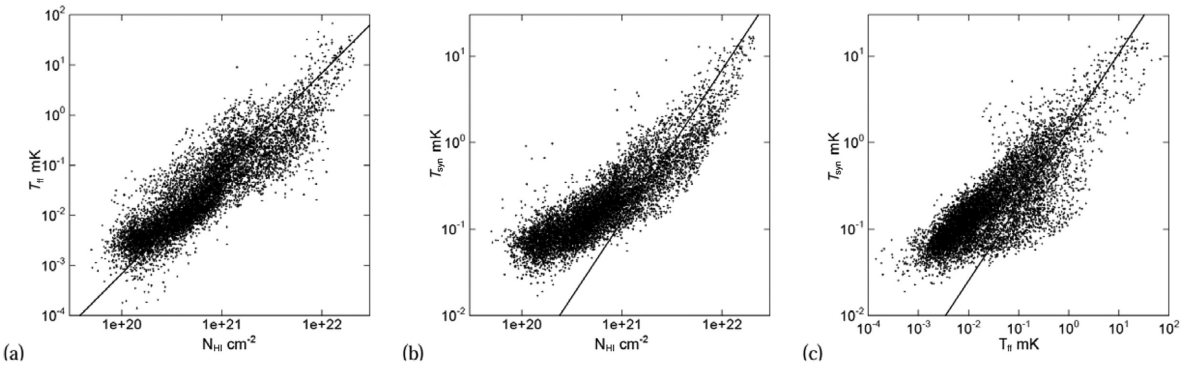

Figure 3. Correlation of $T_{\rm ff}$ and $N_{\rm HI}$ with a line of power index 2, $T_{\rm syn}$ and $N_{\rm HI}$ with a line of index 8/7. Vertical scaling of the lines is arbitrary.

2.2 Correlation among radio observables

2.2.1 Free–free to H I tight relation

Fig. 3(a) shows a plot of $T_{\rm ff}$ against the square of $N_{\rm HI}$. The straight line indicates $T_{\rm ff} \propto N_{\rm HI}^2$, and plots on the log–log space well obey this proportionality. This relation indicates that the thermal electron density $\langle n_{\rm e} \rangle$ is approximately proportional to $\langle n_{\rm HI} \rangle$, if L is not strongly variable from point to point, which is indeed the case, except for the high-$N_{\rm HI}$ region close to the galactic plane. This correlation will be used to estimate the electron density from the H I column.

2.2.2 Synchrotron to ISM relation

Fig. 3(b) is a plot of $T_{\rm syn}$ against $N_{\rm HI}$. The high-intensity region is approximately represented by a power law of index 7/4, $T_{\rm syn} \propto N_{\rm HI}^{7/4}$, as expected from frozen-in magnetic field into the ISM and energy-density equipartition between the magnetic field, cosmic rays, and ISM (see the appendix). The plot of $T_{\rm syn}$ against $T_{\rm ff}$ in Fig. 3(c) shows a similar relation, where $T_{\rm syn} \propto T_{\rm ff}^{7/8}$ is expected from the equipartition, because $N_{\rm HI} \propto T_{\rm ff}^{1/2}$. In both plots, the synchrotron emission tends to exceed the energy equipartition lines at low-intensity regions (high latitudes). This yields a larger uncertainty of the estimated magnetic strength at high latitudes.

2.2.3 RM to ISM relation

Fig. 4 shows plots of the absolute RM values against (a) $N_{\rm HI}$, (b) $T_{\rm syn}$ and (c) $T_{\rm ff}$. It is notable that the plots are more scattered than those in Fig. 3. This is because the rotation measure is an integrated function of the magnetic field strength along the LOS including the reversal of field direction. This scattered characteristic of the RM is

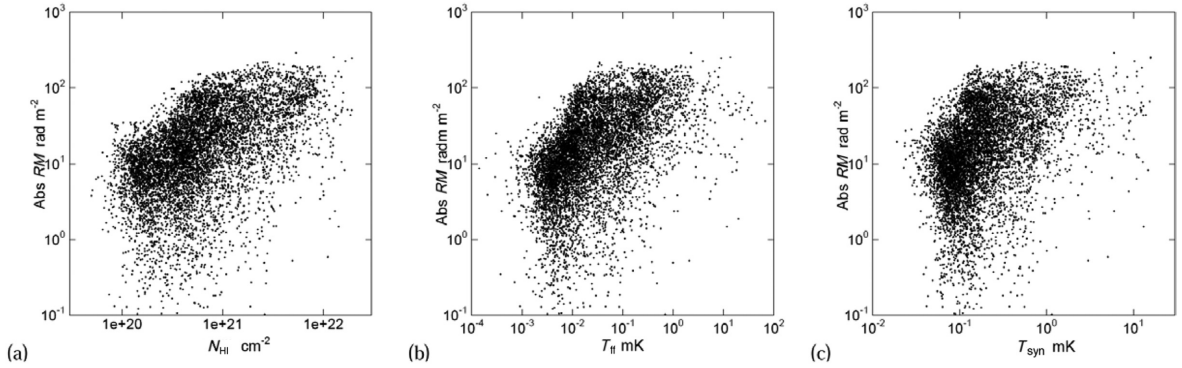

Figure 4. Correlation of $|RM|$ with (a) H I, (b) FF and (c) synchrotron emissions.

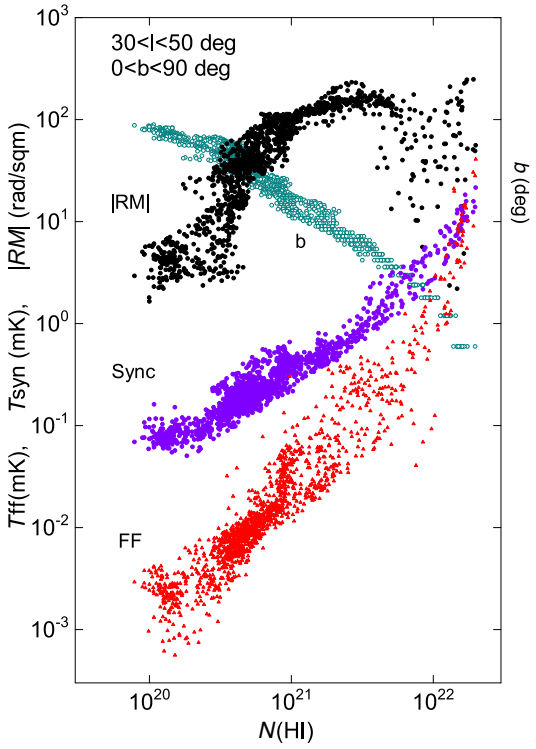

Figure 5. Correlations of $|RM|$, $T_{\rm ff}$ and $T_{\rm syn}$ with $N_{\rm HI}$ in a restricted area on the sky ($30^\circ \leq l \leq 50^\circ$, $b \geq 0^\circ$). Shown by green circles are latitudes with the values indicated by the right axis.

useful to derive the spatial variation of the LOS field direction and strength $B_{//}$.

Although $|RM|$ is scattered against the other ISM observables in the whole-sky data, it may better be correlated in a more narrowly restricted region. Fig. 5 shows an example of plots of $|RM|$, $T_{\rm syn}$ and $T_{\rm ff}$ against $N_{\rm HI}$ in a small area in the first quadrant of the Galaxy at $30^\circ \leq l \leq 50^\circ$ and $b \geq 0^\circ$. Shown by green circles are latitudes corresponding to individual $N_{\rm HI}$ data points, indicating the tight dependence of $N_{\rm HI}$ on the latitude through LOS depths. This figure demonstrates how $|RM|$ is tightly correlated to $N_{\rm HI}$ in a restricted area.

Fig. 6 shows plots of *RM* against galactic latitude and H I column in the first quadrant of the Galaxy. Grey dots show all points, and blue and red dots represent those in two small northern and southern regions in the same quadrant at $30^\circ \leq l \leq 60^\circ$ and $b \geq 10^\circ$ and at $30^\circ \leq l \leq 60^\circ$ and $b \leq -10^\circ$.

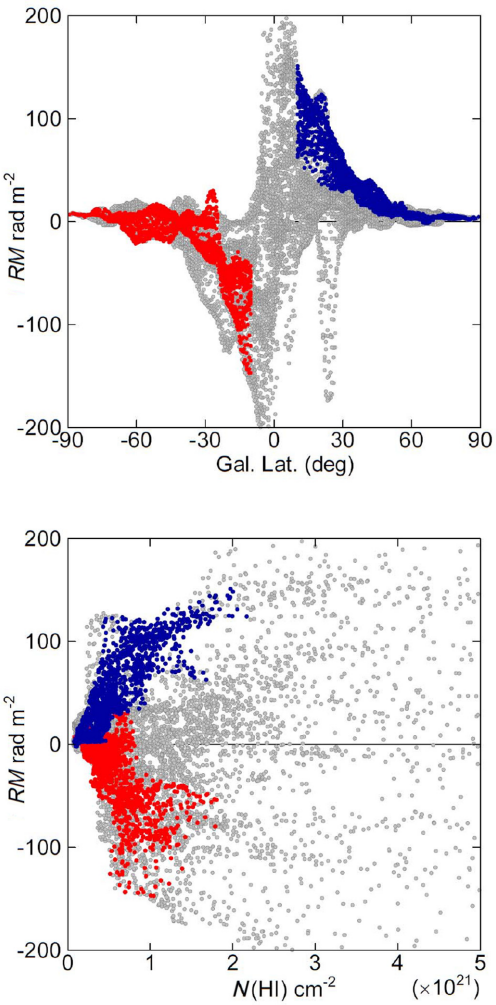

Figure 6. *RM* against galactic latitude (top) and HI column density (bottom) in the first quadrant of the Galaxy. Grey circles show all data points in the first quadrant, blue dots are for a small region at $30^\circ \leq l \leq 60^\circ$ and $b \geq 10^\circ$ and red for $30^\circ \leq l \leq 60^\circ$ and $b \leq -10^\circ$ in the same quadrant.

The absolute RM value increases toward the galactic plane, and the sign of RM changes from negative to positive as the latitude increases, which indicates a sudden reversal of the magnetic field direction. The bottom panel in the figure represents the same phenomenon in terms of the column density of H I gas.

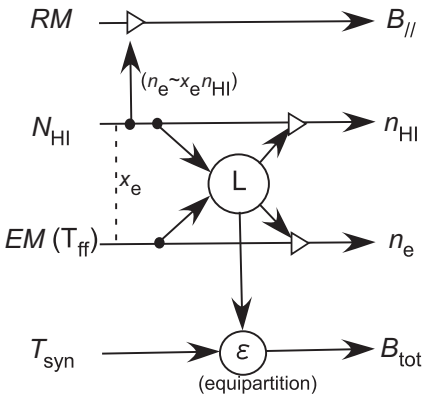

Figure 7. ISM hybrid for determination of physical quantities in the local disc from multiple radio observables.

A linear relation of RM with the H I column is found in low $|RM|$ and $N_{\rm HI}$ regions. However, the linearity is lost toward the galactic plane at $|b| \leq \sim 10^\circ$ with increasing $N_{\rm HI}$. This represents a decrease in the LOS component of magnetic strength $|B_{//}|$ toward the plane, which indicates rapid change of the field direction near the plane.

3 GAS DENSITIES, LINE-OF-SIGHT DEPTH, AND DISC THICKNESS

Given the four radio observables (RM, $T_{\rm ff}$, $T_{\rm syn}$, and $N_{\rm HI}$), four ISM parameters (averaged electron density $\langle n_{\rm e}\rangle \sim x_{\rm e} n_{\rm HI}$, effective LOS depth L, total magnetic intensity B, and LOS component of magnetic field $B_{//}$) can be estimated as follows. Fig. 7 illustrates the flow of the analysis, which we call the ISM hybrid. The effective depth L will be related to the geometrical scale height of the disc through a volume-filling factor.

3.1 Thermal electron density

Thermal electron density is assumed to be proportional to the H I gas density as

$$n_{\rm e} = x_{\rm e} n_{\rm HI}, \tag{9}$$

where $x_{\rm e}$ is the thermal electron fraction in the neutral ISM,

$$x_{\rm e} = \frac{\langle n_{\rm e}\rangle}{\langle n_{\rm e}\rangle + \langle n_{\rm HI}\rangle} \sim \frac{\langle n_{\rm e}\rangle}{\langle n_{\rm HI}\rangle}, \tag{10}$$

which is assumed to be $x_{\rm e} \sim 0.1$ after Foster, Kothes & Brown (2013), who obtained $x_{\rm e} \sim 0.08$. Local H I gas is considered to be in a cold phase from recent measurement of the spin temperature (Sofue 2017, 2018). Even if warm H I is contaminated, its density is an order of magnitude lower, so that the column density is not much affected by warm H I, unless the scale height of warm H I is an order of magnitude greater than that of cold H I.

Electron density is obtained by dividing the emission measure by the column density of electrons, which is related to the H I column, or $n_{\rm e} \sim (n_{\rm e}^2 L)/(n_{\rm e} L) \sim (n_{\rm e}^2 L)/(x_{\rm e} n_{\rm HI} L) \sim EM/(x_{\rm e} N_{\rm HI})$. Thus, we have

$$\left(\frac{\langle n_{\rm e}\rangle}{\rm cm^{-3}}\right) \sim 3.09\times10^{-3}\left(\frac{EM}{\rm pc\ cm^{-6}}\right)\left(\frac{x_{\rm e}N_{\rm HI}}{10^{21}\ \rm cm^{-2}}\right)^{-1}$$
$$\sim 6.82\times10^{2} x_{\rm e}^{-1}\left(\frac{N_{\rm HI}}{10^{21}\ \rm cm^{-2}}\right)^{-1}\left(\frac{T_{\rm ff}}{\rm K}\right)_{23\,\rm GHz} \tag{11}$$

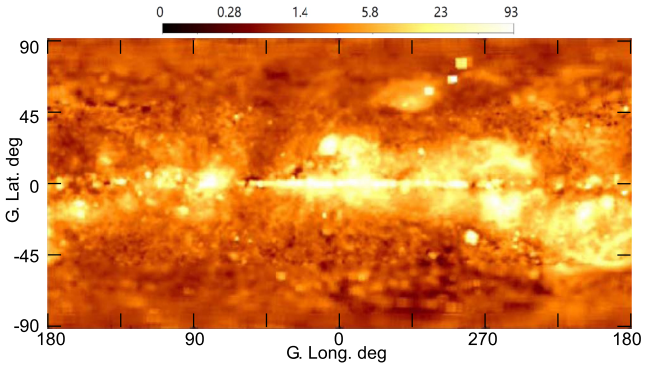

Figure 8. Logarithmic display of the volume density map of H I and thermal electrons. Shown is $\langle n_{\rm HI}\rangle$ [cm^{-3}], which is assumed to be proportional to the thermal electron density as $\langle n_{\rm e}\rangle \sim x_{\rm e}\langle n_{\rm HI}\rangle$ [cm^{-3}] with $x_{\rm e} \sim 0.1$.

at $\nu = 23$ GHz, where the following relations were used. The emission measure is expressed by $T_{\rm ff}$, electron temperature ($T_{\rm e} \sim 10^4$ K), and observing frequency ($\nu = 23$ GHz) as

$$\left(\frac{EM}{\rm pc\ cm^{-6}}\right) = 3.05\times10^{2}\left(\frac{T_{\rm ff}}{K}\right)\left(\frac{T_{\rm e}}{10^4\ \rm K}\right)^{0.35}\left(\frac{\nu}{\rm GHz}\right)^{2.1}$$
$$\sim 2.21\times10^{5}\left(\frac{T_{\rm ff}}{\rm K}\right)_{23\,\rm GHz}, \tag{12}$$

for $T_{\rm e} = 10^4$ K and $\nu = 23$ GHz, where the optical depth is given by (Oster 1961)

$$\tau = 3.28\times10^{-7}\left(\frac{T_{\rm e}}{10^4\ \rm K}\right)^{-1.35}\left(\frac{\nu}{\rm GHz}\right)^{-2.1}\left(\frac{EM}{\rm pc\ cm^{-6}}\right), \tag{13}$$

which is related to $T_{\rm ff}$ for the optically thin case as

$$T_{\rm ff} = (1-{\rm e}^{-\tau})T_{\rm e} \simeq \tau T_{\rm e}. \tag{14}$$

Fig. 8 shows a calculated all-sky map of $n_{\rm HI}$, which is equal to $n_{\rm e}/x_{\rm e}$. The derived H I density at $|b| > \sim 10^\circ$ has nearly a constant value around $\sim 1-2$ cm^{-3}, except for clumpy regions and the Galactic Centre (GC).

3.2 LOS depth, scale height, and volume-filling factor

Recalling that $N_{\rm HI} \sim L n_{\rm HI}$ and $EM \sim L n_{\rm e}^2 \sim L x_{\rm e}^2 n_{\rm HI}^2$, the LOS depth L is given by

$$\left(\frac{L}{\rm pc}\right) \sim 1.05\times10^{5}\left(\frac{x_{\rm e}N_{\rm HI}}{10^{21}\ \rm cm^{-2}}\right)^{2}\left(\frac{EM}{\rm pc\ cm^{-6}}\right)^{-1}$$
$$\sim 0.475\left(\frac{x_{\rm e}N_{\rm HI}}{10^{21}\ \rm cm^{-2}}\right)^{2}\left(\frac{T_{\rm ff}}{\rm K}\right)^{-1}_{23\,\rm GHz}. \tag{15}$$

Fig. 9 shows the derived L plotted against $N_{\rm HI}$ for $x_{\rm e} = 0.1$. The plot roughly obeys the linear relation $N_{\rm HI} \propto L$, indicated by the straight line, while points are largely scattered.

The L defined here is an Àeffective (physical)' LOS depth, and is related to the effective half-thickness (scale height) of the disc, $z_{1/2}$, by

$$L = z_{1/2}\,{\rm cosec}\,|b|. \tag{16}$$

The effective half-thickness is further related to the Àgeometrical'

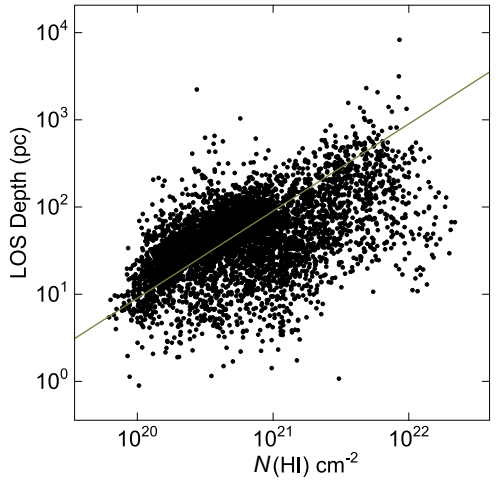

Figure 9. Effective LOS depth L of H I gas for $x_e = 0.1$ plotted against N_{HI}. The straight line indicates a linear relation, $N_{HI} \propto L$, with arbitrary vertical scaling.

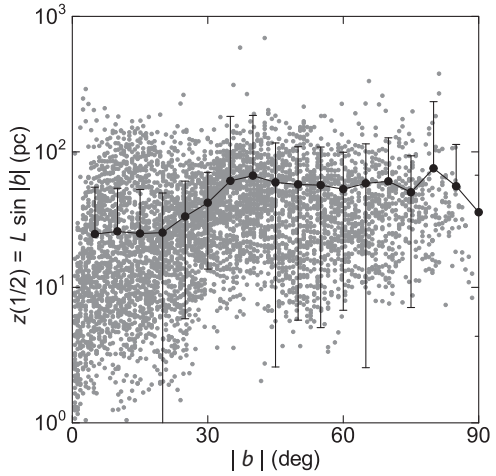

Figure 10. ÀEffective' half-thickness (scale height) of the H I disc defined by $z_{1/2} = L \sin|b|$ plotted against latitude, which is related to the geometrical half-thickness $z_{1/2:disc}$ by $z_{1/2} \sim \eta^{1/3} z_{1/2:disc}$ with η being the volume-filling factor of the gas. Circles are averages of the neighbouring latitude points with standard errors by bars. Points without bars indicate errors greater than the averaged values.

half-thickness

$$z_{1/2} = \eta^{1/3} z_{1/2:disc}, \quad (17)$$

where η is the volume-filling factor of the ISM. The factor η will be determined using these relations referring to independent measurement of the H I disc scale height.

Fig. 10 shows the calculated $z_{1/2}$ against latitude. Original data points are shown by grey dots, and averaged values in latitudinal intervals of $\Delta b = \pm 5^\circ$ are shown by big dots with standard errors. Points without error bars indicate those whose errors are greater than the averaged values. The averaged effective half-thickness tends to a constant of $z_{1/2} \sim 60 \pm 8$ pc at $40^\circ \leq |b| \leq 80^\circ$.

From the current measurements of H I disc half-thickness (160 pc, Lockman et al. 1984; 150 pc, Wouterloot et al. 1990; 200 pc, Levine, Blitz & Heiles 2006; 173 pc, Kalberla et al. 2007; 200 pc, Nakanishi & Sofue 2016; 217 pc, Marasco et al. 2017), we adopt a simple average of the authors' values, $z_{1/2:disc} = 183 \pm 26$ pc. In order for the present determination of $z_{1/2}$ to satisfy equation (17), we obtain $\eta \sim (z_{1/2}/z_{1/2:disc})^3 = 0.035 \pm 0.007$. This value agrees with the recent determination for cold H I gas by Fukui et al. (2018).

4 MAGNETIC FIELDS

4.1 Parallel component

The LOS (or parallel) component of the magnetic field can be obtained by dividing the RM by the column density of thermal electrons as

$$\left(\frac{\langle B_{//}\rangle}{\mu G}\right) \sim 3.81 \times 10^{-3} \left(\frac{RM}{\text{rad m}^{-2}}\right) \left(\frac{x_e N_{HI}}{10^{21}\ \text{cm}^{-2}}\right)^{-1}. \quad (18)$$

It is stressed that this formula yields $\langle B_{//}\rangle$ directly from the observables RM and N_{HI} without employing the LOS depth L. So, $\langle B_{//}\rangle$ is the most accurate quantity determined in this paper.

Equation (18) is particularly simple and useful to estimate the parallel component of the magnetic strength, because it includes only two observables, RM and N_{HI}, where the effective LOS depth L has been cancelled out, leaving x_e as one parameter to be assumed. This relation is now applied for mapping of the $B_{//}$ value on the sky assuming $x_e = 0.1$.

First, the sky is binned into 1° grids in longitude and latitude, and averages are calculated of RM and N_{HI} values within ±1° about each grid point for the $|b| \leq 50^\circ$ region, and within ±2° for $|b| > 50^\circ$. At each point on the grids, $\langle B_{//}\rangle$ is calculated with the aid of equation (18). By this procedure a 361 × 181 meshed map of $\langle B_{//}\rangle$ is obtained on the sky with a resolution of 1–2°.

Fig. 11 shows the thus-obtained all-sky map of $\langle B_{//}\rangle$. Positive values in red indicate a magnetic field away from the observer, and negative ones in blue indicate a field approaching the observer.

Let us remember that the RM map was strongly affected by the peaked line-of-sight depth near the galactic plane, causing large positive and negative values near the plane. This caused a steep latitudinal gradient in the RM due to the field reversal from north to south, resulting in RM singularity along the galactic plane.

On the other hand, the $\langle B_{//}\rangle$ map is not affected by the LOS depth, so that it exhibits the field strength and direction only, so that the RM singularity along the galactic plane does not appear. The map reveals a widely extended arched region with a positive magnetic strength of $\langle B_{//}\rangle \sim +5$ μG in the north from $(l, b) \sim (40^\circ, 5^\circ)$ to $(210^\circ, 0^\circ)$. This arch seems to be continued by a negative strength arch with $\langle B_{//}\rangle \sim -5$ μG in the south from $(l, b) \sim (50^\circ, -5^\circ)$ to $(160^\circ, -30^\circ)$.

It may be possible to connect the positive and negative $B_{//}$ arches to draw a giant loop, or a shell, from $l \sim 40^\circ$ to 220° with the field direction being reversed from north to south. Alternatively, the positive arch may be traced through the empty sky around the south pole in the present data (Taylor et al. 2009), where the improved map shows positive RM (Oppermann et al. 2012). If this is the case, the RM arches may trace a sinusoidal belt from the Southern hemisphere in the first and second quadrants to the Northern in the third and fourth quadrants, drawing an ∞-shaped belt on the sky, with the necks in the galactic plane at $l \sim 30^\circ$ and 240°. The arched magnetic region along the Aquila Rift from $(l, b) \sim (30^\circ, -10^\circ)$ to $(300^\circ, +30^\circ)$ with $\langle B_{//}\rangle \sim +2$ to -4 μG could be a part of the ∞ belt.

It is also interesting to note that both the northern and southern polar regions show positive $B_{//}$ with $\langle B_{//}\rangle \sim +1$ μG, indicating that the vertical (zenith) field directions are pointing away from the Sun.

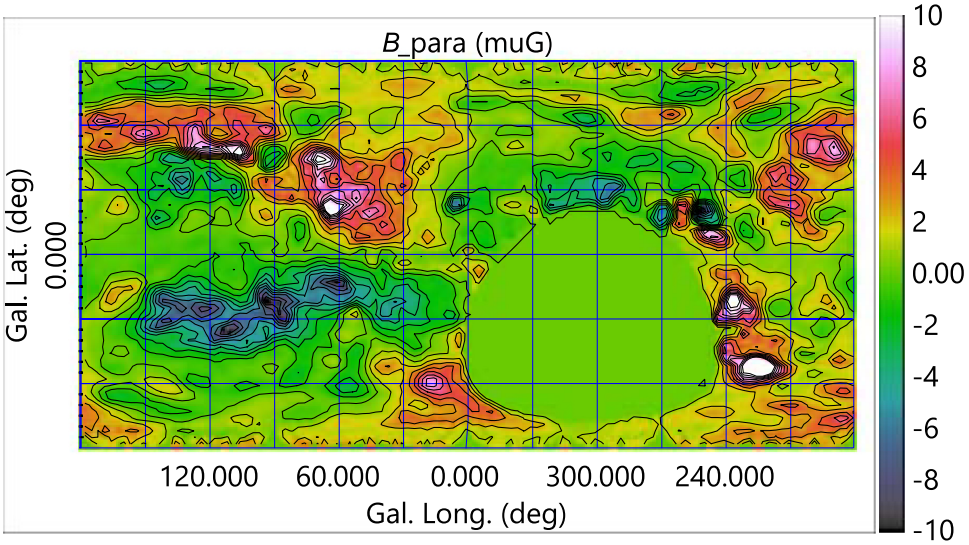

Figure 11. All-sky maps of $\langle B_{//}\rangle$ with contours at intervals of 1 μG. Positive values in red indicate a field away from the observer, negative ones in blue indicate one approaching.

4.2 Total intensity

The total magnetic intensity $B_{\rm tot}$ is calculated by assuming that the magnetic and cosmic ray energy densities are in equipartition as (see the appendix)

$$B^2/8\pi \sim N_{\rm CR} E_{\rm cr}, \tag{19}$$

where $N_{\rm CR}$ is the cosmic ray electron number density and $E_{\rm cr}$ is the representative energy of radio-emitting cosmic rays. The magnetic strength is then related to the frequency ν and volume emissivity ϵ as

$$\left(\frac{\langle B_{\rm tot}\rangle}{\mu{\rm G}}\right) \sim 3.03\times10^{8} Q \left(\frac{\nu}{\rm GHz}\right)^{-1/7} \epsilon^{2/7}, \tag{20}$$

where Q is an equipartition factor, which depends on various assumed conditions and source models. There have been decades of discussion about Q since Burbidge (1956), which includes dependence on such parameters as the spectral index, cut-off frequencies, proton-to-electron density ratio, volume-filling factor, field orientation, and/or degree of alignment (e.g. Beck & Krause 2005). The emissivity ϵ is related to L and $T_{\rm syn}$ through equation (5):

$$\left(\frac{\epsilon}{\rm erg\ cm^{-3}\ s^{-1}}\right) \sim 6.796\times10^{-12} \left(\frac{T_{\rm syn}}{\rm K}\right) \left(\frac{\nu}{\rm GHz}\right)^{3} \left(\frac{L}{\rm pc}\right)^{-1} \tag{21}$$

The emissivity depends on the filling factor through $\epsilon \propto L^{-1} \propto \eta^{-1/3}$. So, we here introduce an η-corrected magnetic strength:

$$\mathscr{B}_{\rm tot} \sim \eta^{2/21} \langle B_{\rm tot}\rangle / Q. \tag{22}$$

For $\eta \sim 0.035$ as measured in the previous section, we obtain $\mathscr{B}_{\rm tot} \sim 0.73 \langle B_{\rm tot}\rangle / Q$.

Fig. 12 shows an all-sky map of the calculated total magnetic intensity $\langle B_{\rm tot}\rangle/Q$. Except for discrete radio sources including radio spurs and GC, the map shows a smooth local magnetic intensity within ∼200 pc. Local magnetic strengths were calculated in intermediate-latitude regions at $+30^\circ \le b \le +70^\circ$ and $-70^\circ \le b \le -30^\circ$ to obtain $B_{\rm tot}/Q = 10.7 \pm 3.1$ μG and 10.3 ± 2.7 μG, respectively. Combining the two regions, we obtain $B_{\rm tot}/Q = 10.5 \pm 3.0$ μG. By correcting for the volume-filling factor ($\eta^{2/21} = 0.73$), we obtain a representative local field strength of $\mathscr{B}_{\rm tot} = 7.6 \pm 2.1$ μG for $Q = 1$.

Given the $\langle B_{\rm tot}\rangle$ and $\langle B_{//}\rangle$ maps, the perpendicular component of the magnetic field is easily calculated by $\langle B_{\perp}\rangle \sim \sqrt{\langle B_{\rm tot}\rangle^2 - \langle B_{//}\rangle^2}$. However, the accuracy of the above-estimated $\langle B_{\rm tot}\rangle$ is too poor to obtain a meaningful map of the perpendicular component.

5 DISCUSSION

5.1 Summary

The latitudinal plots in Fig. 2 indicate that the four observables, *RM*, $T_{\rm syn}$, $T_{\rm ff}$, and $N_{\rm HI}$, are tightly correlated with each other through their cosec $|b|$ variations. This indicates that the distributions of the sources and their physical parameters are also tightly correlated with each other. Based on this fact, the sources of these emissions and Faraday rotation are assumed to be distributed in a single local disc in the Galaxy.

On this assumption, some useful relations were derived for calculating the local ISM quantities such as magnetic strength $\langle B_{\rm tot}\rangle$, and LOS component of the magnetic field $\langle B_{//}\rangle$, thermal electron density $\langle n_{\rm e}\rangle$, H I density $\langle n_{\rm HI}\rangle$, and LOS depth L, or the scale thickness $z_{1/2}$ and $z_{1/2:{\rm disc}}$ with the volume-filling factor η. It was emphasized that the determination of L plays an essential role in the present hybrid method to calculate the physical quantities, while only $\langle B_{//}\rangle$ can be directly calculated from *RM* and $N_{\rm HI}$ without being affected by L.

Applying the method to archival radio data, all-sky maps of $\langle B_{//}\rangle$ and $\langle B_{\rm tot}\rangle$ were obtained, which revealed a detailed magnetic structure in the local interstellar space within the Galactic disc near the Sun. The $\langle B_{//}\rangle$ map showed that the magnetic direction varies sinusoidally along a giant arch-shaped belt on the sky, changing its LOS direction from north to south and vice versa every two galactic quadrants. The maximum parallel component of ∼± 5–6 μG was observed on the belt at intermediate latitudes. The $\langle B_{\rm tot}\rangle$ map showed that the total magnetic strength is smoothly distributed on the sky, and the averaged value was obtained to be

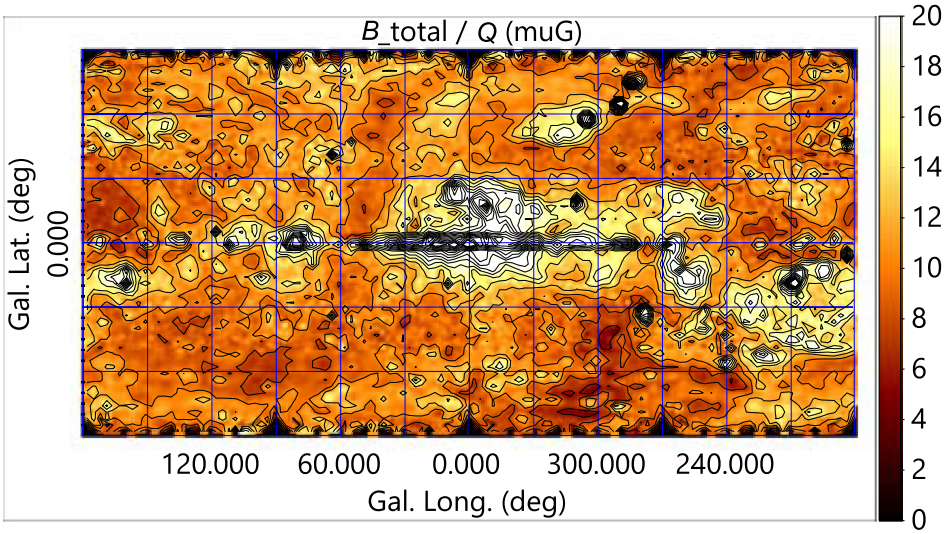

Figure 12. All-sky maps of $\langle B_{\rm tot}\rangle/Q$ with contours at intervals of 2 μG. The η-corrected strength is obtained by $\mathscr{B}_{\rm tot} \sim 0.72\times$ map values.

$\langle B_{\rm tot}\rangle/Q \sim 10.5$ μG in the intermediate-latitude region. Assuming an equipartition factor of $Q = 1$, we obtained an η-corrected field strength of $\mathscr{B}_{\rm tot} \sim 7.6$μG for the measured volume-filling factor of $\eta \sim 0.035$.

5.2 Dependence on the thermal electron fraction

The proportionality of the densities of thermal electrons and H I gas is confirmed through the tight correlation between $N_{\rm HI}$ and $T_{\rm ff}$ (EM) by Figs 2 and 3. On this basis, we assumed a constant thermal electron fraction of $x_{\rm e} \sim 0.1$ close to the current measurement on the order of ∼0.08 (Foster et al. 2013). However, $x_{\rm e}$ affects the result through equation (17), where $L \propto x_{\rm e}^2$, and it propagates to the other quantities as $\langle B_{//}\rangle \propto x_{\rm e}^{-1}$, $\langle B_{\rm tot}\rangle \propto x_{\rm e}^{-4/7}$, $\langle n_{\rm e}\rangle \propto x_{\rm e}^{-1}$, and $\langle n_{\rm HI}\rangle \propto x_{\rm e}^{-2}$. Namely, the ISM quantities are generally inversely proportional to $x_{\rm e}$, with the strongest effect on $\langle n_{\rm HI}\rangle$ and the weakest on $\langle B_{\rm tot}\rangle$.

5.3 Uncertainty from energy equipartition

The most uncertain point in the present analysis is the estimation of magnetic strength from the energy equipartition of cosmic ray electrons and magnetic field. Since the equipartition factor Q is still open to discussion, the obtained total magnetic intensities should be taken only as a reference to see the relative distribution of the strength on the sky.

Also, the single disc assumption for synchrotron and thermal components may break at high latitudes. As in Fig. 3, the plots of $T_{\rm syn}$ against $N_{\rm HI}$ and $T_{\rm ff}$ bend at high latitudes, showing an order-of-magnitude excess at high latitudes over smooth extension from the disc component. The synchrotron excess over that expected from the frozen-in assumption is about $\delta T_{\rm syn} \sim 0.1$ K.

In Fig. 13 we plot $T_{\rm syn} - \delta T_{\rm syn}$, mimicking *halo-subtracted* synchrotron emission, which is well fitted by a power law expected from low- and intermediate-latitude regions. This fact suggests that the energy equipartition holds inside the disc, whereas a non-thermal halo at the ∼0.1 mK level at 23 GHz is extending outside the gas disc.

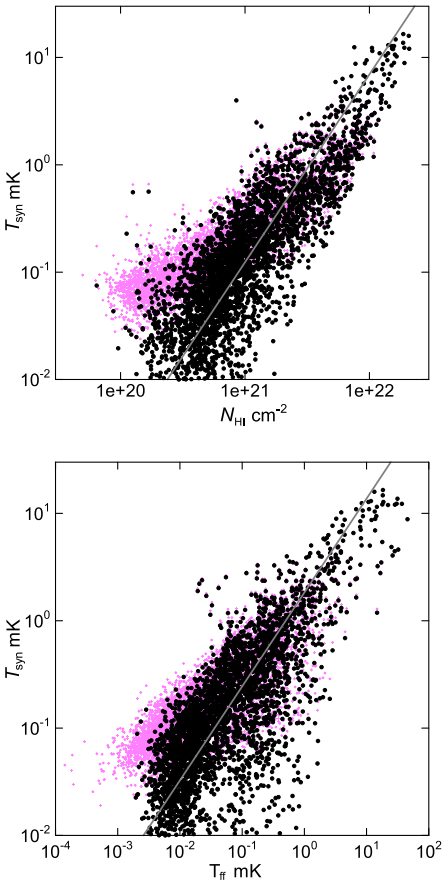

Figure 13. Correlation of $T_{\rm syn} - 0.1$ mK with $N_{\rm HI}$ and $T_{\rm ff}$, which are approximately represented by a power law of index 7/4 and 7/8, respectively. Vertical scaling of the lines is arbitrary. Original data are shown in violet.

5.4 Effect of inhomogeneity

From the tight cosec $|b|$ relation of the radio observables used, for which no extinction problem exists, we assumed a uniform layered disc of ISM. In more realistic conditions, however, the layer may

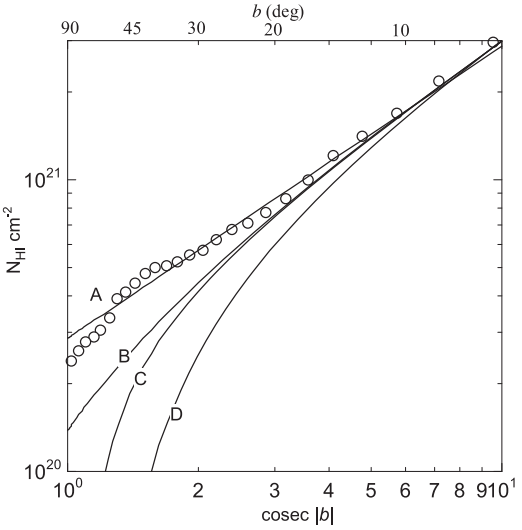

Figure 14. Cosec $|b|$ relation of the H I disc from Fig. 2 (averaged values every 2° by circles) compared with (A) a model of a Gaussian disc of scale height 200 pc without a bubble; (B) the same disc with a spherical bubble of radius 100 pc; (C) and (D) discs with vertical cylindrical cavities of radii 100 and 200 pc, respectively. Values are normalized to the observation at $b \sim 5°$.

be more or less not uniform, and the assumption made in equations (6)–(8) may not hold, or must be modified.

However, it is emphasized that Àclumpy' inhomogeneity does not affect the Àeffective' LOS depth L by definition, because L already includes the volume-filling factor. Hence, the determined values of the ISM, which are averages of values Àinside' the clumps (or within L), are not affected by the inhomogeneity.

The assumption made for equations (6)–(8) will not hold exactly in a disc with globally varying density with the height. For example, if the functions f and g are represented by a Gaussian function of the height from the galactic plane, we have $\langle f \rangle \sim 1.1 \langle f^2 \rangle^{1/2}$ and $\langle fg \rangle \sim 1.2 \langle f \rangle \langle g \rangle$. For a $\cosh^{-2}$ function, as for self-gravitating disc, the factors are 1.2 and 1.4, respectively. These factors propagate on to the results, yielding uncertainty by a factor of ∼1.1–1.2 for quantities having linear dependence on the distance, and by 1.2–1.4 to those with non-linear dependence such as *RM* and *EM*. However, the finally determined B and n_e or n_{HI} are more linearly dependent on the distance, and hence their uncertainties may be about a factor of ∼1.1–1.2 at most.

5.5 Local bubble

A large-scale irregularity of the ISM has been reported as a local bubble (Bochkarev 1992; Lallement et al. 2003; Liu et al. 2017; Alves et al. 2018), which makes a cavity around the Sun of radius $r_{bub} \sim 100$–200 pc widely open to the galactic halo. Then, a difficulty is encountered to explain the tight cosec $|b|$ relation in Fig. 2. In order for the cosec relation to hold up to $b \sim \pm 80°$ at least, the scale height of the galactic disc must be greater than $\sim r_{bub} \tan 80°$ ∼ 600 pc to 1.2 kpc, which is obviously not the case. If the disc scale height is ∼200 pc as measured in H I, the open cavity should result in huge empty sky in radio around the galactic poles, which also appears not to be the case.

In Fig. 14 we compare the cosec $|b|$ relation observed for N_{HI} with cavity models mimicking the local bubble. Line A indicates a Gaussian disc of scale height 200 pc without a bubble; B represents a case with a spherical bubble of radius 100 pc in a Gaussian disc of scale height 200 pc, and C and D cylindrical cavities of radii 100 and 200 pc, respectively. Model C may be compared with the result by Lallement et al. (2003), which appears significantly displaced from the cosec $|b|$ relation. Such is found not only in H I, but also in thermal and synchrotron emissions, and the Faraday RM (Fig. 2). Therefore, the relation between the local bubble and the cosec $|b|$ disc in radio remains a question.

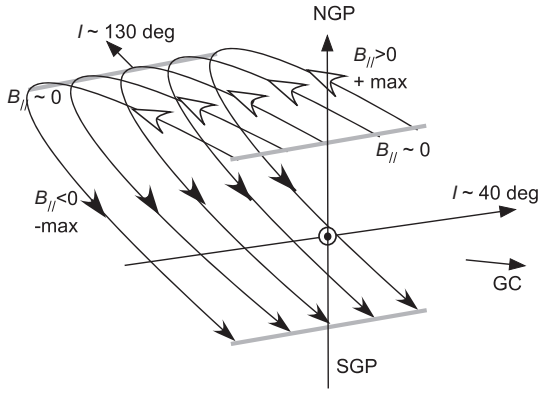

Figure 15. Possible topology of local magnetic lines of force to explain the $B_{//}$ map in Fig. 11 (NGP/SGP = North/South Galactic Poles).

5.6 Other observables

Molecular gas has not been taken into account in this study, because the nearest molecular clouds within LOS depths concerned in this paper are rather few (Knude & Hog 1998). Comparison with a local bubble surrounded by dusty clouds (e.g. Lallement et al. 2003), besides the cosec $|b|$ problem, would be an interesting subject, although the present analysis gives only averaged values along the LOS within L, and hence cannot be directly compared with a 3D study.

Polarization data in radio and infrared observations were not used, although they are obviously useful to improve the present hybrid analysis. Inclusion of these observables is beyond the scope of this paper, for which more sophisticated analyses would be required.

5.7 Local magnetic topology

Despite the various uncertainties as above, we emphasize that the projected topology of $B_{//}$ mapped in Fig. 11 is rather certain. Although the ∝-shaped variation of *RM* might sound a bit strange, we could speculate on the possible topology of the magnetic lines of force in the local space.

The field direction reverses about the galactic plane from north to south in a wide range from $l \sim 30$–210°. The $B_{//}$ value attains its maximum and minimum at both intermediate latitudes around $(l, b) \sim (130°, \pm 30$–$50°)$. Such *RM* behaviour on the sky could be explained by a reversed topology of the local field, as illustrated in Fig. 15.

ACKNOWLEDGEMENTS

We thank the authors of the LAB H I survey (Dr Kalberla et al.), the all-sky rotation measure map (Dr Taylor et al.), and the *WMAP*

seven-year maps (Dr Gold et al.) for the archival data. The data analyses were performed on a computer system at the Astronomical Data Center of the National Astronomical Observatories of Japan.

REFERENCES

Akahori T. et al., 2018, PASJ, 70, R2
Alves M. I. R., Boulanger F., Ferrière K., Montier L., 2018, A&A, 611, L5
Beck R., Krause M., 2005, Astron. Nachrichten, 326, 414
Bochkarev N. G., 1992, Astron. Astrophys. Trans., 3, 3
Burbidge G. R., 1956, ApJ, 124, 416
Foster T., Kothes R., Brown J. C., 2013, ApJ, 773, L11
Fukui Y., Hayakawa T., Inoue T., Torii K., Okamoto R., Tachihara K., Onishi T., Hayashi K., 2018, ApJ, 860, 33
Gold B. et al., 2011, ApJS, 192, 15
Kalberla P. M. W., Burton W. B., Hartmann D., Arnal E. M., Bajaja E., Morras R., Pöppel W. G. L., 2005, A&A, 440, 775
Kalberla P. M. W., Dedes L., Kerp J., Haud U., 2007, A&A, 469, 511
Knude J., Hog E., 1998, A&A, 338, 897
Lallement R., Welsh B. Y., Vergely J. L., Crifo F., Sfeir D., 2003, A&A, 411, 447
Landau L. D., Lifshitz E. M., 1971, in The Classical Theory of Fields, 3rd edn. Pergamon Press, Oxford, Ch. 9
Levine E. S., Blitz L., Heiles C., 2006, ApJ, 643, 881
Liu W. et al., 2017, ApJ, 834, 33
Lockman F. J., 1984, ApJ, 283, 90
Mao S. A. et al., 2012, ApJ, 755, 21
Marasco A., Fraternali F., van der Hulst J. M., Oosterloo T., 2017, A&A, 607, A106
Moffet A. T., 1975, in Sandage A., , Kristian J. et al., eds, Galaxies and the Universe: Stars and Stellar Systems. Chicago Univ. Press, Chicago, Vol. 9, Ch. 7
Nakanishi H., Sofue Y., 2016, PASJ, 68, 5
Oppermann N. et al., 2012, A&A, 542, A93
Oster L., 1961, AJ, 66, 50
Sofue Y., 2017, MNRAS, 468, 4030
Sofue Y., 2018, PASJ, 70, 50
Sofue Y., Fujimoto M., Wielebinski R., 1986, ARA&A, 24, 459
Sofue Y., Nakanishi H., 2017, MNRAS, 464, 783
Stil J. M., Taylor A. R., Sunstrum C., 2011, ApJ, 726, 4
Sun X. H. et al., 2015, ApJ, 811, 40
Taylor A. R., Stil J. M., Sunstrum C., 2009, ApJ, 702, 1230
Van Eck C. L. et al., 2017, A&A, 597, A98
Wolleben M. et al., 2010, ApJ, 724, L48
Wouterloot J. G. A., Brand J., Burton W. B., Kwee K. K., 1990, A&A, 230, 21

APPENDIX A: EQUIPARTITION

A1 B, E, and $N(E)$ by ϵ and ν

The equipartition between magnetic and cosmic ray pressure relates the magnetic strength B, representative energy E and density $N(E)$ of cosmic ray electrons responsible for synchrotron emission at the observing frequency ν and volume emissivity ϵ (Burbidge 1956; Moffet 1975; Sofue et al. 1986 for review). We here write down the basic relations between B, $N(E)$ and E, which are used to calculate the Àreference value' of B for $Q = 1$ in equation (20):

$$\frac{B^2}{8\pi} \sim EN(E), \tag{A1}$$

$$\nu \sim \frac{e}{4\pi m_e^3 c^5} BE^2, \tag{A2}$$

and

$$\epsilon \sim -\frac{\mathrm{d}E}{\mathrm{d}t} N(E) \sim \frac{2e^4}{3m_e^4 c^7} B^2 E^2\, N(E) \tag{A3}$$

(e.g. Landau & Lifshitz 1971). These equations can be solved for B in terms of ν and ϵ as

$$\left(\frac{B}{\mu\mathrm{G}}\right) \sim 3.03 \times 10^8 \left(\frac{\nu}{\mathrm{GHz}}\right)^{-1/7} \left(\frac{\epsilon}{\mathrm{erg\ cm^{-3}\ s^{-1}}}\right)^{2/7}. \tag{A4}$$

Moffet (1975) gave a coefficient 3.25×10^8 for a radio spectral index of $\alpha = -0.75$.

As a by-product, we obtain

$$\left(\frac{N(E)}{\mathrm{cm^{-3}}}\right) \sim 2.91 \times 10^9 \left(\frac{\nu}{\mathrm{GHz}}\right)^{-6/7} \left(\frac{\epsilon}{\mathrm{erg\ cm^{-3}\ s^{-1}}}\right)^{5/7}, \tag{A5}$$

and

$$\left(\frac{E}{\mathrm{erg}}\right) \sim 1.26 \times 10^{-6} \left(\frac{\nu}{\mathrm{GHz}}\right)^{4/7} \left(\frac{\epsilon}{\mathrm{erg\ cm^{-3}\ s^{-1}}}\right)^{-1/7}. \tag{A6}$$

A2 $T_{\rm syn}$ by $N_{\rm HI}$

Using equations (4), (A1) and (A2), $T_{\rm syn}$ is expressed in terms of L and B as

$$T_{\rm syn} \propto LB^{9/2}. \tag{A7}$$

Assuming that the H I gas has a constant velocity dispersion ($\sigma \sim$ constant) and is in pressure (energy-density) balance with the magnetic field as

$$\frac{B^2}{8\pi} \sim \frac{1}{2} m_{\rm H} n_{\rm HI} \sigma^2 \propto n_{\rm HI}, \tag{A8}$$

we have

$$B \propto n_{\rm HI}^{1/2} \sim (N_{\rm HI}/L)^{1/2}. \tag{A9}$$

Inserting this into equation (A7),

$$T_{\rm syn} \propto n_{\rm HI}^{1/4} N_{\rm HI}^{7/4}. \tag{A10}$$

While the column density $N_{\rm HI}$ is highly variable with b and L, the volume density $n_{\rm HI}$ is not, and appears by a weak power of index 1/4. So, we may approximate $T_{\rm syn}$ by

$$T_{\rm syn} \propto N_{\rm HI}^{7/4}. \tag{A11}$$

This paper has been typeset from a TEX/LATEX file prepared by the author.